JJMIE

Jordan Journal of Mechanical and Industrial Engineering

A Nonlinear Kinostatic Optimization Synthesis for Circumduction Generation Exoskeleton

Ahmad Al-Jarrah [1] , Yahia Al-Smadi [2,3]

[1] *Department of Mechatronics Engineering, The Hashemite University, Zarqa, Jordan*
[2] *Department of Mechanical Engineering, Jordan University ofScience and Technology, Irbid, Jordan.*
[3] *Department of Electromechanical Engineering Technology, Abu Dhabi Polytechnic, UAE*

Abstract

Rehabilitation is necessary for those with restricted arm mobility to enhance arm movement efficiency and offer dynamic stability. Recent research initiatives are aimed at supporting the rehabilitation of individuals with disabilities or injuries that limit arm movement. Accordingly, the RRSS (Revolute-Revolute-Spherical-Spherical) exoskeleton mechanism for circumduction motion is proposed in this study. The objective is to ascertain the parameters of the mechanism required to accomplish or approximate a sequence of prescribed circumduction positions. When a rigid body needs to operate according to a precise displacement sequence, this design is appropriate which is considered as a nonlinear kinostatic optimization problem. The problem can be formulated with constraints concerning driven link buckling, driver static torque, and driver elastic deflection. The suggested RRSS circumduction motion production process is used to simulate and analyze the workspace of the arm and shoulder as well as muscle activity.

Significant changes in the reactions of the muscles, bones, and joints movement were noted during virtual testing of the suggested exoskeleton on a human arm. Some tremendous results of exoskeleton joints and human arm fusion were found. Some computations were made for the deltoid muscles, which control arm movement in the scapular plane, the FCU (Flexor Carpi Ulnaris) muscle, which is located in the forearm and controls hand flexion and adduction, and the caput breve, a short head of biceps brachii muscles.

Keywords: Exoskeleton Mechanism, Motion Generation, Optimization, Rehabilitation, Static Torque, Deflection, Buckling.

1. Introduction

The glenoid cavity of the scapula is relatively shallow, and the head of the humerus is relatively big, making the glenohumeral joint, a synovial ball and socket joint, quite unstable. As a result, it is a very mobile joint in the body with three major motions: rolling, sliding, and spinning, which translate into clinical motions for the arm, including internal and external rotation, flexion and extension in the front plane, abduction and adduction in the sagittal plane, and circumduction, which combines the motions mentioned above.

Rehabilitation processes are becoming more and more advanced and innovative for those who are suffering from low motor skills performance, especially stroke patients. Upper limb exoskeletons have been the subject of many projects, which have produced models in a variety of sizes and shapes for medical, military, and commercial purposes. Only the exoskeleton kinostatic design of neuromuscular rehabilitation for the arms and shoulders will be covered in this study. As an example of rehabilitation exoskeletons, the ABLE platform [1] was created using a cable-driven actuation system with a 4 DOF specification. Patients are trained to achieve passive motion using a semi-exoskeleton robot called the ARMin exoskeleton model[2]. Exoskeletons, both active and passive, that are employed in rehabilitation processes are shown in [3-7].

Additional examples of upper limb rehabilitation exoskeletons can be seen in [8 -14], where the exoskeleton dynamics for paraplegic rehabilitation is in [15]. The systems mentioned above used a variety of actuation techniques, such as cable actuation [7], parallel mechanisms [9], gearmotors [10], linkages [13], hydraulic[16] or pneumatic cylinders [8], rotary pneumatic actuators [13], and pneumatic muscle actuators [13]. Other technologies were introduced besides the exoskeleton design, such as inertia compensation [17], sensing & control [18], enhancing ergonomics [19], preventing hyperstaticity [20], and organizing rehabilitation treatment [21-22].

A major drawback of all exoskeletons mentioned before is that they are all bulky and rely on too many moving parts. The proposed mechanism is simple and can be proven practically for rehabilitation treatment. Unlike the parallel shoulder mechanism reported in[23], the proposed spatial mechanism presented in Figure 1 can be synthesized using

---

* Corresponding author e-mail: ...

a motion generation technique to simulate and approximate the circumduction motion of the shoulder. Motion generation synthesis is accomplished by the given four prescribed rigid-body positions defined in the x, y, and z-coordinates of variables **p**, **q**, **r**, and **s**, and then calculating the mechanism parameters x, y, and z-coordinates of fixed pivot variables **a₀** and **b₀** and moving pivot variables **a₁** and **b₁**.

Motion generation is a well-established field for spatial RRSS four-bar mechanisms, robotics, and manipulators [24-26]. Recent contributions of synthesizing mechanisms have been established with consideration of the driving torque. This work is considered an extension of the author's work described in Al-smadi et al [27-28] where kinostatic optimization problem was modeled and analyzed for planar four-bar motion generation with prescribed static torque, rigid-body reaction force, and structural constraints. Russell et al [29] studied the motion generation of RRSS and applied the principle of virtual work to obtain the crank driving torque, Haijun et al [30] classified the motion of RRSS and other spatial mechanisms based on the linkages dimension, and Lee and Yoon [31]synthesized RRSS mechanism using Euler parameters and quaternion algebra. The robust design of parallel spherical robots was examined by Al-Widyan et al. [32], whereas manipulators with six degrees of freedom were studied in [33-35]. Also, Hashlamon [36] and Gong et al [37] studied parallel mechanisms. Qaiyum [38], Nguyen-Van et al[39],and El-Shakery et al [40] have focused on optimization in their mechanism synthesis whereas Lee et al [41] examined the adjustable crank length on four-bar motion generation.
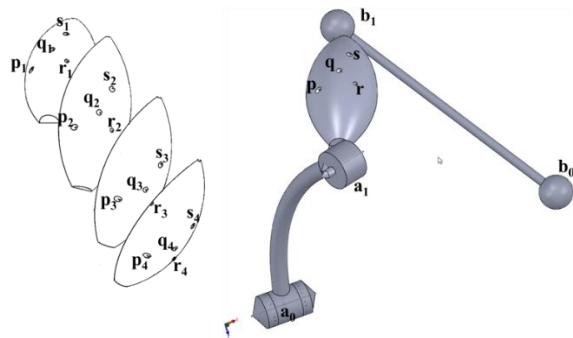

Figure 1. Prescribed rigid-body positions and calculated RRSS mechanism.

A rudimentary model of a medical exoskeleton suit is presented in this study to help patients regain motor abilities in their upper extremities. It is also regarded as a training aid for their muscular activities. The mechanism parameters required to achieve or approximate a set of prescribed rigid-body positions can be calculated using conventional motion generation methods (Suh and Radcliffe [42]). Although such solutions are useful for preliminary kinematic analysis, other factors (e.g., static loads, dynamic loads, stresses, strains, etc.) must be considered before manufacturing the physical prototype of the mechanical design. This work considers static driving link torque given a rigid-body load. By integrating the new static torque constraint into conventional RRSS mechanism motion generation models (Suh and Radcliffe [42]), spatial mechanisms are synthesized to achieve prescribed rigid-body positions and to satisfy driver static torque for a given rigid-body load.

2. Conventional Spatial Motion Generation

The spatial motion generation model proposed by Suh and Radcliffe [42] is covered by equations (1-3). The "constant length" constraints in equations (1) and (2) guarantee the constant lengths of linkages **a₀a₁** and **b₀b₁**. The prescribed scalar lengths of links **a₀a₁** and **b₀b₁** are represented by the variables L_1 and L_2 in equations (1) and (2), respectively. Equation (3) is a rigid-body spatial displacement matrix. When using this conventional spatial mechanism synthesis model to calculate the coordinates of the fixed pivots **a₀** and **b₀** and the moving pivots **a₁** and **b₁**(where **a₀**= [a_{0x}, a_{0y}, a_{0z}, 1], **a₁** = [a_{1x}, a_{1y}, a_{1z}, 1], **b₀** = [b_{0x}, b_{0y}, b_{0z}, 1] and **b₁** = [b_{1x}, b_{1y}, b_{1z}, 1]), the user can specify a maximum of five rigid-body poses when five variables are specified.

$$\left(\left[\mathbf{D}_{1j}\right]\mathbf{a}_1 - \mathbf{a}_0\right)^T \left(\left[\mathbf{D}_{1j}\right]\mathbf{a}_1 - \mathbf{a}_0\right) - L_1^2 = 0 \qquad (1)$$

$$\left(\left[\mathbf{D}_{1j}\right]\mathbf{b}_1 - \mathbf{b}_0\right)^T \left(\left[\mathbf{D}_{1j}\right]\mathbf{b}_1 - \mathbf{b}_0\right) - L_2^2 = 0 \qquad (2)$$

$$\left[\mathbf{D}_{1j}\right] = \begin{bmatrix} p_{jx} & q_{jx} & r_{jx} & s_{jx} \\ p_{jy} & q_{jy} & r_{jy} & s_{jy} \\ p_{jz} & q_{jz} & r_{jz} & s_{jz} \\ 1 & 1 & 1 & 1 \end{bmatrix} \begin{bmatrix} p_{jx} & q_{jx} & r_{jx} & s_{jx} \\ p_{jy} & q_{jy} & r_{jy} & s_{jy} \\ p_{jz} & q_{jz} & r_{jz} & s_{jz} \\ 1 & 1 & 1 & 1 \end{bmatrix}^{-1} \qquad (3)$$

Where *j= 1, 2, 3, 4,5.*

The points (**p**, **q**, **r**, and **s**) on the coupler body are defined in traditional motion generation; the subscripts *1* and *j* denote the starting and displaced poses respectively. The displacement matrix [**D₁ⱼ**] of equation (3) becomes proportional with proportional rows if the coupler points lie on the same line (prohibited); this matrix cannot be inverted.

3. Driver Link Static Torque

When the rigid-body of the spatial RRSS mechanism is subjected to an external load **F**, a driving link torque **T** brings about static equilibrium. The load **F** is applied at the arbitrary rigid-body point **q** as shown in Figure 2a. As a concept, including the structural conditions in motion generation is not commonly established. Other than the work of Huang and Roth [43], who created analytical models of motion generation for planar four-bar mechanisms with a given rigid-body load, most other studies that investigate the structural behavior of mechanisms under load neglect to take into account the behavior in the motion generation. In planar four-bar mechanisms, contributions to motion generation with structural conditions are covered in [27-28]. Referring to Figure 2, to formulate the crank static torque constraint, the moment condition ΣM=0 is considered about the unit vector **u**ₐ₀ of the crank link fixed revolute joint; hence, the torque will be

$$\mathbf{T} + (\overrightarrow{\mathbf{a}_0\mathbf{q}} \times \mathbf{F}).\vec{\mathbf{u}}_{a0} + (\overrightarrow{\mathbf{a}_0\mathbf{b}_0} \times \mathbf{R}_b).\vec{\mathbf{u}}_{a0} = 0 \qquad (4)$$

As illustrated in Figure 2(c), the fixed pivot reaction forces on the links **R**ₐ₀ and **R**ᵦ₀ are also considered in the moment condition. The resulting equation of the moments about the moving pivot revolute joint unit vector **u**ₐ₁ at equilibrium is

$$(\overrightarrow{\mathbf{a}_1\mathbf{b}_1} \times \mathbf{R}_b).\vec{\mathbf{u}}_{a1} - (\overrightarrow{\mathbf{a}_1\mathbf{q}} \times \mathbf{F}).\vec{\mathbf{u}}_{a1} = 0 \qquad (5)$$

613

Since link $\mathbf{b}_0\mathbf{b}_1$ is a two-force member, vectors $\mathbf{R}_{b1}$ and $\overrightarrow{b_0b_1}$ are collinear and that gives

$$\mathbf{R}_b = R_b \frac{\overrightarrow{b_0b_1}}{\left|\overrightarrow{b_0b_1}\right|} \quad (6)$$

And the reaction load R_b is a real number that varies with the mechanism driver position. Substituting equation (6) into (5) and solving for R_b, equation (5) becomes

$$R_b = \frac{(\overrightarrow{a_1q} \times \mathbf{F}).\vec{u}_{a1}}{(\overrightarrow{a_1b_1} \times \overrightarrow{b_0b_1}).\vec{u}_{a1}} \cdot \left|\overrightarrow{b_0b_1}\right| \quad (7)$$

Now using the force condition $\Sigma\mathbf{F}=0$ at equilibrium for the coupler, then re-arrange for $\mathbf{R}_{a1}$ gives

$$\mathbf{R}_{a1} = \mathbf{F} - \frac{(\overrightarrow{a_1q} \times \mathbf{F}).\vec{u}_{a1}}{(\overrightarrow{a_1b_1}).\vec{u}_{a1}} \quad (8)$$

Rearranging the moment condition $\Sigma\mathbf{M}=0$ in equation (4), and substituting equations (6) and (7) into equation (4) gives

$$\mathbf{T}+(\overrightarrow{a_0q} \times \mathbf{F}).\vec{u}_{a0}+\left(\frac{(\overrightarrow{a_1q} \times \mathbf{F}).\vec{u}_{a1}}{(\overrightarrow{a_1b_1} \times \overrightarrow{b_0b_1}).\vec{u}_{a1}}(\overrightarrow{a_0b_0} \times \overrightarrow{b_0b_1})\right).\vec{u}_{a0} = 0 \quad (9)$$

The required driving torque to achieve equilibrium of the crank for any pose is

$$\mathbf{T}_i=(\overrightarrow{a_0q} \times \mathbf{F}).\vec{u}_{a0}+\left(\frac{(\overrightarrow{a_1q} \times \mathbf{F}).\vec{u}_{a1}}{(\overrightarrow{a_1b_1} \times \overrightarrow{b_0b_1}).\vec{u}_{a1}}(\overrightarrow{a_0b_0} \times \overrightarrow{b_0b_1})\right).\vec{u}_{a0} \quad (10)$$

Where $i = 1, 2, 3, ..., N, j = 1, 2, 3, ..., N,$
$\overrightarrow{a_1q}=\mathbf{q}_j -\left[\mathbf{D}_{1j}\right]\mathbf{a}_1, \overrightarrow{a_0a_1}=\left[\mathbf{D}_{1j}\right]\mathbf{a}_1 -\mathbf{a}_0,$
$\overrightarrow{b_0b_1}=\left[\mathbf{D}_{1j}\right]\mathbf{b}_1 -\mathbf{b}_0,$ and $\overrightarrow{a_1b_1}=\left[\mathbf{D}_{1j}\right]\left(\mathbf{b}_1 -\mathbf{a}_1\right)$

It is important to note that the mechanism represented in Figure 2a was modeled using the SolidWorks program, and the ADAMS solver plane was used to carry out the kinostatic analysis with an arbitrary load in the y-z plane. The kinostatic equilibrium result is displayed in Figure 2d, where the arrow size is the result of the ADAMS solution. The figure shows that the follower link is under coaxial compression load, and the crank link is under bending load, both of which are greater in value than the compressive load at the follower link.

Equation (10) calculates the RRSS mechanism crank static torque for a given rigid-body force. Expressing

equation (10) as an inequality constraint to limit the maximum crank static torque (τ_{max}) for N prescribed coupler posesyields

$$(T_j)^\mathrm{T}(T_j) < \tau_{max}^2 \quad (11)$$

where $j = 1,2,3,...,N$.

While planar mechanisms in static positions with rigid-body loads are taken into consideration in Huang and Roth work [43], the spatial effect of link deflection and buckling resulting from the rigid-body loads-structural responses is not taken into consideration. This will compromise the structural integrity of the mechanism and, consequently, the accuracy of the precision positions achieved. Using the virtual work principle, Russell et al. [29] calculated the static torque, equation (12), for the RRSS mechanism. After testing equations 10 and 12, the outcomes were remarkably comparable to one another. The stiffness matrix formulation for the spatial mechanism will be the main topic of the following section.

The stiffness of crank and follower links under loading will affect the achieved pose locations and must be calculated and considered when achieving the final pose locations.

4. RRSS Mechanism Deflection Model Under Rigid-body Load

A statically-loaded spatial RRSS mechanism deflection model is demonstrated in Figure 3 where a load $\{\mathbf{F}\}$ is applied at point $\mathbf{q}$ of the rigid body mechanism. The static deflections $\{\mathbf{U}\}$ of the moving pivots $\mathbf{a}_1$ and $\mathbf{b}_1$ and the rigid-body points $\mathbf{p}$, $\mathbf{q}$, $\mathbf{r}$, and $\mathbf{s}$can be calculated using the analytical model of equation (13). In equation (13), the global stiffness matrix $\left[\mathbf{K}_{global}\right]$includes an element stiffness matrix (equation14) for each mechanism link. The element stiffness matrix for link $\mathbf{a}_0\mathbf{a}_1$ and the rigid-body (link $\mathbf{a}_1\mathbf{q}\mathbf{b}_1$) is given by equation (16) [44-45]. Because link $\mathbf{b}_1\mathbf{b}_0$ is a two-force member (and therefore under columnar loading only), its element stiffness matrix $\left[\mathbf{k}_{axial}\right]$ is given by equation (17) [44-45]. Equation (15) transforms each local element coordinate frame to the global coordinate frame by rotating each element node by the associated element angle θ_j [44-45].

$$T_j = -\mathbf{F}.\left\{-\frac{(\mathbf{b}_j -\mathbf{b}_0)^T\left\{\left[P_{u_0}\right](\mathbf{b}_j -\mathbf{a}_0)\right\}}{(\mathbf{b}_j -\mathbf{b}_0)^T\left\{\left[P_{u_j}\right](\mathbf{b}_j -\mathbf{a}_j)\right\}}\left[P_{u_j}\right].(\mathbf{q}_j -\mathbf{a}_j)+\left[P_{u_0}\right].(\mathbf{q}_j -\mathbf{a}_0)\right\} \quad (12)$$
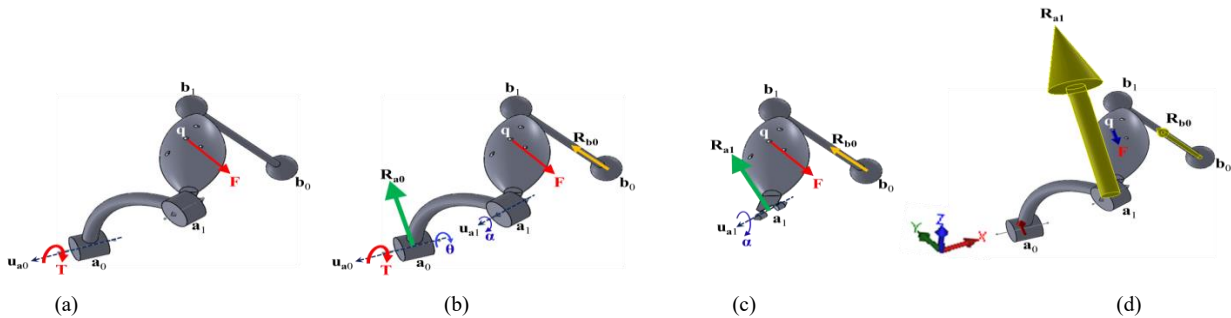

Figure 2. Spatial RRSS mechanism (a) in static equilibrium, (b) with reaction forces $\mathbf{R}_{a0}$ and $\mathbf{R}_{b0}$, (c) with reaction forces $\mathbf{R}_{b0}$ and $\mathbf{R}_{a1}$ and (d) ADAMS result for an arbitrary proposed loading

Variables E_i, A_i, J_i, G_i, I_i, and L_i in Figure 3 (where $i=1,2,3,4$) are the modulus of elasticity, cross-sectional area, polar moment of inertia, shear modulus, moment of inertia, and length of each link respectively. Due to the assumption that link $\mathbf{a_1qb_1}$ is a uniform rigid-body, $E_2=E_3$, $A_2=A_3$, $I_2=I_3$ and its modulus of elasticity is significantly higher (in this work, 10^6 times higher) than those of link $\mathbf{a_0a_1}$ and link $\mathbf{b_1b_0}$. Link $\mathbf{a_1qb_1}$ becomes almost rigid in the spatial four-bar mechanism deflection model when such a big modulus is specified.   The orientation of each link is denoted by angles θ_l (where i=1,2,3,4) shown in Figure 4. These angles are taken into consideration for each link end pivot and are utilized in the transformation matrix $\left[\mathbf{M}_{trans_j}\right]$ (equation 15).
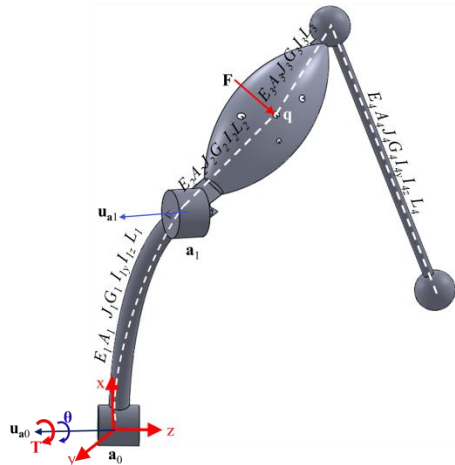

Figure 3. Statically-loaded RRSS deflection model mechanism

$$\{\mathbf{F}\} = \left[\mathbf{K}_{global}\right]\{\mathbf{U}\} \tag{13}$$

$$\left[\mathbf{K}_j\right] = \left[\mathbf{M}_{trans_j}\right]\left[\mathbf{k}_j\right]\left[\mathbf{M}_{trans_j}\right]^{-1} \tag{14}$$

$$\left[\mathbf{M}_{trans_j}\right] = \begin{bmatrix} \lambda_{3\times3} & & & \\ & \lambda_{3\times3} & & \\ & & \lambda_{3\times3} & \\ & & & \lambda_{3\times3} \end{bmatrix} \tag{15}$$

where

$$\lambda = \begin{bmatrix} C_{\hat{x}x} & C_{\hat{y}x} & C_{\hat{z}x} \\ C_{\hat{x}y} & C_{\hat{y}y} & C_{\hat{z}y} \\ C_{\hat{x}z} & C_{\hat{y}z} & C_{\hat{z}z} \end{bmatrix} \quad and \quad C:\cos\theta$$
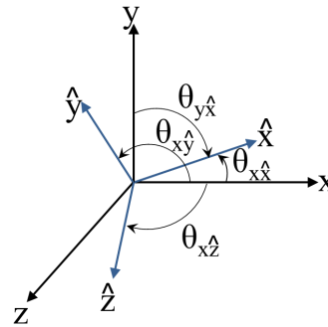

Figure 4. Direction cosines associated with x-axis

$$[\mathbf{k}_j] = \begin{bmatrix}
\frac{A_jE_j}{L_j} & 0 & 0 & 0 & 0 & 0 & -\frac{A_jE_j}{L_j} & 0 & 0 & 0 & 0 & 0 \\
0 & \frac{12E_jI_{jz}}{L_j^3} & 0 & 0 & 0 & \frac{6E_jI_{jz}}{L_j^2} & 0 & -\frac{12E_jI_{jz}}{L_j^3} & 0 & 0 & 0 & \frac{6E_jI_{jz}}{L_j^2} \\
0 & 0 & \frac{12E_jI_{jy}}{L_j^3} & 0 & -\frac{6E_jI_{jy}}{L_j^2} & 0 & 0 & 0 & -\frac{12E_jI_{jy}}{L_j^3} & 0 & -\frac{6E_jI_{jy}}{L_j^2} & 0 \\
0 & 0 & 0 & \frac{G_jJ_j}{L_j} & 0 & 0 & 0 & 0 & 0 & -\frac{G_jJ_j}{L_j} & 0 & 0 \\
0 & 0 & -\frac{6E_jI_{jy}}{L_j^2} & 0 & \frac{4E_jI_{jy}}{L_j} & 0 & 0 & 0 & \frac{6E_jI_{jy}}{L_j^2} & 0 & \frac{2E_jI_{jy}}{L_j} & 0 \\
0 & \frac{6E_jI_{jz}}{L_j^2} & 0 & 0 & 0 & \frac{4E_jI_{jz}}{L_j} & 0 & -\frac{6E_jI_{jz}}{L_j^2} & 0 & 0 & 0 & \frac{2E_jI_{jz}}{L_j} \\
-\frac{A_jE_j}{L_j} & 0 & 0 & 0 & 0 & 0 & \frac{A_jE_j}{L_j} & 0 & 0 & 0 & 0 & 0 \\
0 & -\frac{12E_jI_{jz}}{L_j^3} & 0 & 0 & 0 & -\frac{6E_jI_{jz}}{L_j^2} & 0 & \frac{12E_jI_{jz}}{L_j^3} & 0 & 0 & 0 & -\frac{6E_jI_{jz}}{L_j^2} \\
0 & 0 & -\frac{12E_jI_{jy}}{L_j^3} & 0 & \frac{6E_jI_{jy}}{L_j^2} & 0 & 0 & 0 & \frac{12E_jI_{jy}}{L_j^3} & 0 & \frac{6E_jI_{jy}}{L_j^2} & 0 \\
0 & 0 & 0 & -\frac{G_jJ_j}{L_j} & 0 & 0 & 0 & 0 & 0 & \frac{G_jJ_j}{L_j} & 0 & 0 \\
0 & 0 & -\frac{6E_jI_{jy}}{L_j^2} & 0 & \frac{2E_jI_{jy}}{L_j} & 0 & 0 & 0 & \frac{6E_jI_{jy}}{L_j^2} & 0 & \frac{4E_jI_{jy}}{L_j} & 0 \\
0 & \frac{6E_jI_{jz}}{L_j^2} & 0 & 0 & 0 & \frac{2E_jI_{jz}}{L_j} & 0 & -\frac{6E_jI_{jz}}{L_j^2} & 0 & 0 & 0 & \frac{4E_jI_{jz}}{L_j}
\end{bmatrix} \tag{16}$$

$$[\mathbf{k}_{axial}] = \begin{bmatrix} \frac{A_j E_j}{L_j} & 0 & 0 & 0 & 0 & 0 & -\frac{A_j E_j}{L_j} & 0 & 0 & 0 & 0 & 0 \\ 0 & 0 & 0 & 0 & 0 & 0 & 0 & 0 & 0 & 0 & 0 & 0 \\ 0 & 0 & 0 & 0 & 0 & 0 & 0 & 0 & 0 & 0 & 0 & 0 \\ 0 & 0 & 0 & 0 & 0 & 0 & 0 & 0 & 0 & 0 & 0 & 0 \\ 0 & 0 & 0 & 0 & 0 & 0 & 0 & 0 & 0 & 0 & 0 & 0 \\ 0 & 0 & 0 & 0 & 0 & 0 & 0 & 0 & 0 & 0 & 0 & 0 \\ -\frac{A_j E_j}{L_j} & 0 & 0 & 0 & 0 & 0 & \frac{A_j E_j}{L_j} & 0 & 0 & 0 & 0 & 0 \\ 0 & 0 & 0 & 0 & 0 & 0 & 0 & 0 & 0 & 0 & 0 & 0 \\ 0 & 0 & 0 & 0 & 0 & 0 & 0 & 0 & 0 & 0 & 0 & 0 \\ 0 & 0 & 0 & 0 & 0 & 0 & 0 & 0 & 0 & 0 & 0 & 0 \\ 0 & 0 & 0 & 0 & 0 & 0 & 0 & 0 & 0 & 0 & 0 & 0 \\ 0 & 0 & 0 & 0 & 0 & 0 & 0 & 0 & 0 & 0 & 0 & 0 \end{bmatrix} \quad (17)$$

5. Link Buckling and Elastic Deflection Constraints

As previously mentioned, since the follower link $\mathbf{b}_1\mathbf{b}_0$ is a two-force member, it is solely subjected to columnar loading. Critical buckling load for a column with pinned ends is calculated using Euler's formula as follows

$$P_{cr} = \frac{\pi^2 EI}{L^2} \quad (18)$$

and Johnson's critical buckling load formula [44] for the same system is

$$P_{cr} = \sigma_y \left(A - \frac{\sigma_y L^2}{4\pi^2 EI} \right) \quad (19)$$

where variables E, I, and L are the modulus of elasticity, moment of inertia, and effective column length respectively. In equation (19), variables A and σ_y are the column cross-section area and material yield stress respectively.

Using Euler's formula to express equation (2) as an inequality constraint to forbid link $\mathbf{b}_1\mathbf{b}_0$ buckling for N prescribed rigid-body poses yields

$$\left(\left[\mathbf{D}_{1j} \right] \mathbf{b}_1 - \mathbf{b}_0 \right)^T \left(\left[\mathbf{D}_{1j} \right] \mathbf{b}_1 - \mathbf{b}_0 \right) < \frac{\pi^2 EI}{R_b} \quad (20)$$

where $j = 1,2,3,...,N$.

Noting that the right-side term L^2 in equation (18) and the scalar columnar load R_b in link $\mathbf{b}_1\mathbf{b}_0$ (equation (6)) become the critical buckling load. Solving for L^2 in equation (19) and substituting the right-side term in inequality constraint (20) results in a buckling constraint based on Johnson's formula. Because the right-side term in inequality constraint (20) is the squared scalar length of link $\mathbf{b}_1\mathbf{b}_0$, this link is constrained to a length that is less than the buckling length.

It is important to mention that the follower link $\mathbf{b}_1\mathbf{b}_0$ is displayed as straight in the earlier figures. However, if this link is curved, then the effects of initial out-of-straightness must be considered. This is also accentuated in unsymmetrical column sections [46].

Since link $\mathbf{a}_0\mathbf{a}_1$ is not a two-force member, it is not subjected to columnar loading only, in contrast to link $\mathbf{b}_1\mathbf{b}_0$. Because this link is held in static equilibrium by a torque of about $\mathbf{u}_{a0}$, there is also a transverse load component acting on link $\mathbf{a}_0\mathbf{a}_1$. In this work, the buckling of link $\mathbf{a}_0\mathbf{a}_1$ is not explicitly considered because the link stiffness required to limit transverse deflection is generally sufficient to avoid link buckling (especially as the maximum permissible transverse deflection becomes smaller). Moreover, link $\mathbf{a}_0\mathbf{a}_1$ is a fixed-end cantilevered beam under a load with a transverse component as shown in figures 2b, 2d, and 3. As a result, constraining the deflection of link $\mathbf{a}_0\mathbf{a}_1$ is critical because of the loading conditions and constraints on the link, which make link deflection a common occurrence. The Euler formula for the deflection of a fixed-end cantilevered beam [44] is

$$\delta = \frac{PL^3}{3EI} \quad (21)$$

where variables P, L, $E,$ and I are the free-end transverse load, beam length, modulus of elasticity, and moment of inertia respectively. Equation (8) gives the total load on the moving revolute pivot $\mathbf{a}_1$; hence, the transverse component of this load is

$$\overrightarrow{R_{a_{trans}}} = \left(-\frac{\left| \overrightarrow{a_1 q} \times \mathbf{F} \right|}{\left| \overrightarrow{a_1 b_1} \times \overrightarrow{b_1 b_0} \right|} \overrightarrow{b_1 b_0} - \mathbf{F} \right) \times \frac{\overrightarrow{a_0 a_1}}{\left| \overrightarrow{a_0 a_1} \right|} \quad (22)$$

Expressing equation (1) as an inequality constraint to limit crank deflection for N prescribed rigid-body poses yields

$$\left(\left[\mathbf{D}_{1j} \right] \mathbf{a}_1 - \mathbf{a}_0 \right)^T \left(\left[\mathbf{D}_{1j} \right] \mathbf{a}_1 - \mathbf{a}_0 \right) < \left(\frac{3\delta EI}{\left| \overrightarrow{R_{a_{trans}}} \right| L} \right) \quad (23)$$

where $j = 1,2,3,...,N$ and the right-side term is L^2 in equation (21).

In addition to specifying variables E and I in equation (23), the user will also specify a transverse deflection-to-link length ratio δ/L. Because the right-side term in equation (23) is the squared scalar length of link $\mathbf{a}_0\mathbf{a}_1$, this link is constrained to a length that produces a maximum static deflection which is less than the specified maximum static deflection.

6. Motion Generation Nonlinear Optimization Problem

Combining equations (1) and (3) into a single objective function that accommodates an unlimited number of N sets of prescribed path generation parameters to be minimized yields

$$f(\mathbf{X}) = \sum_{i=2}^{N} \left\{ \left[\left(\left[\mathbf{D}_{1i} \right] \mathbf{a}_1 - \mathbf{a}_0 \right)^T \left(\left[\mathbf{D}_{1i} \right] \mathbf{a}_1 - \mathbf{a}_0 \right) - L_1^2 \right]^2 + \left(\left[\mathbf{D}_{1j} \right] \mathbf{b}_1 - \mathbf{b}_0 \right)^T \left(\left[\mathbf{D}_{1j} \right] \mathbf{b}_1 - \mathbf{b}_0 \right) \left[-L_2^2 \right]^2 \right\} \quad (24)$$

where $\mathbf{X} = \left(a_{0x}, a_{0y}, a_{0z}, a_{1x}, a_{1y}, a_{1z}, L_1, b_{0x}, b_{0y}, b_{0z}, b_{1x}, b_{1y}, b_{1z}, L_2 \right)^T$. Equation (24) and inequality constraints of equations (11), (20) and (23) constitute a nonlinear optimization problem. Solving this problem will give mechanism solutions that approximate the prescribed rigid-body poses and satisfy maximum driver static torque, maximum driver elastic deflection, and driven link buckling conditions.

SQP (Sequential Quadratic Programming) is the algorithm used to solve this nonlinear optimization issue, which is a nonlinear constraints problem. It uses the Quasi-Newton approach to solve its QP (Quadratic Programming) sub-problem and line search approach to determine the iteration step. The merit function used by Han [47] and Powell [48] is used in the following form

$$\Psi(\mathbf{X}) = f(\mathbf{X}) + \sum_{k=1}^{m} r_k \max\left[0, g_k(\mathbf{X})\right] \quad (25)$$

where $g_k(\mathbf{X})$ represents each inequality constraint, m is the total number of inequality constraints, and the inequality constraint penalty parameter is

$$r_k = (r_{l+1})_k = \max_k\left\{\lambda_k, \frac{1}{2}\left((r_l)_k + \lambda_k\right)\right\} \quad (26)$$

The value of r for successive minimizations can be found as

$$r_l = (\text{FAC})^{1-\text{IR}} \quad (27)$$

where IR=1 at the start and is incremented by 1 after each successive suboptimum is found. The factor FAC can be set arbitrarily although it is recommended to be 10 for normal use [42]. l in equation (26) is the iteration index for calculating the penalty parameter r_k for each inequality constraint ($l=0, 1, 2, 3,…$). The Lagrange multiplier, which is the rate of the change of the objective function being optimized with respect to the constraint variables, is

$$\lambda_k = \frac{\nabla f(\mathbf{X})}{\nabla g_k(\mathbf{X})} \quad (28)$$

After specifying initial guesses for the unknown variables in the nonlinear optimization problem $(\mathbf{X})$, the SQP algorithm is employed to calculate the unknown variables using the flowchart shown in Figure 5. The loop in the flowchart is repeated until the penalty term in equation (25), $\sum_{k=1}^{m} r_k \max\left[0, g_k(\mathbf{X})\right]$, is less than a specified penalty term residual ε; where ε is selected to be 0.001 for the example in this work.

Like other optimization algorithms, SQP algorithm does not guarantee global optimization. The quality of the initial guesses could determine whether the algorithm converges, and to what values. The author employed computer-aided drafting software to assist in specifying the initial guesses. Drafting and superimposing the prescribed rigid-body precision positions in 3-D space enabled the authors to determine likely locations (and subsequently likely initial guesses) for the fixed and moving pivots.

The author utilized MathCAD, a commercial mathematical analysis package with built-in SQP, instead of codifying the SQP algorithm as a stand-alone application. Other commercial mathematical analysis software such as Mathematica and Matlab also include nonlinear optimization problem solvers like SQP.The nonlinear optimization problem formulated and presented in this work ran efficiently in MathCAD with run times measured in seconds.
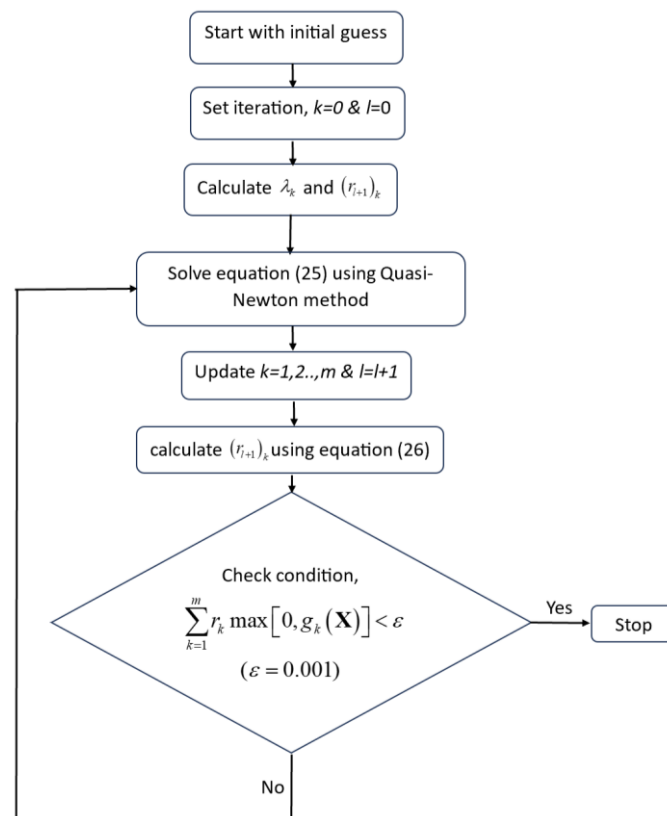

Figure 5. SQP flowchart

7. Example Problem

Because the crank and follower links are flexible, the deflections of these links simultaneously compromise the rigid body poses and rigid-body loads, maximum driver torque, and maximum driver deflection values (including Young's modulus and moment of inertia data for the crank and follower). Planar four-bar mechanisms are synthesized using the model formulated in this work. In the following demonstrated example, the synthesized planar four-bar mechanism approximated each of the eight prescribed rigid-body poses below the specified maximum driver static torque, below the maximum specified crank static deflection, and without follower buckling for the given coupler load.

Table 1 includes the *xyz*-coordinates (in inches) of eight prescribed coupler poses. This is nearly twice the maximum number of prescribed displacements available with the conventional motion generation method included in this work [42]. The maximum allowed crank torque is $\tau_{max}= 350$ lbf.in and the coupler force at *q* is $F = (0, -100, 0)^T$ lbf. The crank and follower links shall be constructed of solid circular steel ($E = 29 \times 10^6$ psi, $G = 11.3 \times 10^6$ psi) tubing of 3/8in and 1/8 in diameters, respectively. This example assumes that the links will be constructed of 'off-the shelf' steel bars of standard sizes (as opposed to custom-made bars

where the moment of inertia could be a design variable).The coupler link is assumed to be rigid. For each prescribed coupler pose, the maximum crank deflection shall not exceed 1/16 in, and avoiding follower buckling is critical.

Using the motion generation goal program on the proposed RRSS rehab mechanism with initial guesses of a_0=(0, 0,0), a_1=(1.5, 2.5,2), b_0=(6.5, 0.5,2) and b_1=(7.5, 4,1), the calculated solution is a_0=(0.3627, 0.0188), a_1=(1.7838, 2.3355), b_0=(6.4932, 1.1458) and b_1=(7.5854, 4.4303). Because the crank and follower links are flexible, the deflections of these links simultaneously compromise the accuracy of the rigid-body poses achieved by the synthesized mechanism. Table 2 shows the achieved coordinates for coupler points **p**, **q**, **r**, and **s.** Figure 6 illustrates the synthesized motion generator. Table 3 includes the resulting static torque and deflection of the crank link as well as the resulting follower link columnar loads after incorporating the parameters of the synthesized mechanism in the mechanism deflection model in Section 3. Figure7 includes a plot of the scalar difference between the prescribed and achieved rigid-body poses. Rigid-body poses 1 through 8 along with their associated driver static torque (Figure 8) correspond to crank displacement angles of $\delta\theta_1$=0°, 21.4313°, 40.6595°, 60.2763°, 79.4361°, 98.6439°, 118.2737° and 137.7683°.

Table 1. Prescribed Rigid-body Positions (f=100 lbf, τ_4=350 lbf.in)

	p	q	r	s
Pose 1	0.6963, 3.1255, 1.9702	0.7949, 3.1796, 2.2813	1.2335, 3.4429, 2.3310	1.0601, 3.1743, 2.5299
Pose 2	0.8120, 2.2729, 2.7521	0.9495, 2.2595, 3.0527	1.4249, 2.4517, 3.0865	1.2354, 2.1774, 3.2616
Pose 3	0.9022, 1.2241, 3.1811	1.0810, 1.149, 3.4491	1.5735, 1.2952, 3.4335	1.3849, 1.0107, 3.5926
Pose 4	0.9571, 0.1172, 3.2333	1.1739, -0.0070, 3.4501	1.6631, 0.1324, 3.3772	1.4907, -0.1732, 3.5140
Pose 5	0.9793, -0.9207, 2.9373	1.2261, -1.0773, 3.0922	1.6985, -0.9071, 2.9826	1.5506, -1.2404, 3.0766
Pose 6	0.9811, -1.7936, 2.3572	1.2476, -1.9670, 2.4482	1.7002, -1.7464, 2.3448	1.5754, -2.1011, 2.3663
Pose 7	0.9772, -2.4408, 1.5677	1.2533, -2.6206, 1.5967	1.6930, -2.3588, 1.5492	1.5821, -2.7099, 1.4701
Pose8	0.9766, -2.8239, 0.6367	1.2536, -3.0015, 0.6032	1.6919, -2.7366, 0.6462	1.5825, -3.0412, 0.4536

Table 2. Rigid-body Positions Achieved by RRSS Mechanism

	p	q	r	s
Pose 1	0.6963, 3.1255, 1.9702	0.7949, 3.1796, 2.2813	1.2335, 3.4429, 2.3310	1.0601, 3.1743, 2.5299
Pose 2	0.8143, 2.2519, 2.7653	0.9526, 2.2371, 3.0654	1.4287, 2.4279, 3.0984	1.239, 2.1535, 3.2731
Pose 3	0.9046, 1.1878, 3.1888	1.0847, 1.1109, 3.4554	1.5774, 1.2561, 3.4379	1.3891, 0.9711, 3.5964
Pose 4	0.9576, 0.1021, 3.2314	1.1748, -0.0226, 3.4475	1.664, 0.1169, 3.3739	1.4919, -0.189, 3.5103
Pose 5	0.979, -0.8933, 2.9499	1.2251, -1.0492, 3.1066	1.6981, -0.8803, 2.9975	1.5494, -1.2128, 3.0931
Pose 6	0.981, -1.741, 2.4039	1.2468, -1.9137, 2.4992	1.7006, -1.6966, 2.3939	1.5745, -2.0503, 2.4213
Pose 7	0.9774, -2.3949, 1.6423	1.2531, -2.5745, 1.6766	1.6935, -2.3151, 1.6226	1.5819, -2.6679, 1.553
Pose 8	0.9764, -2.7952, 0.7457	1.2537, -2.9736, 0.7192	1.6916, -2.7065, 0.7513	1.5827, -3.0188, 0.5713

Table 3. Crank static torques, deflections, and follower link columnar loads

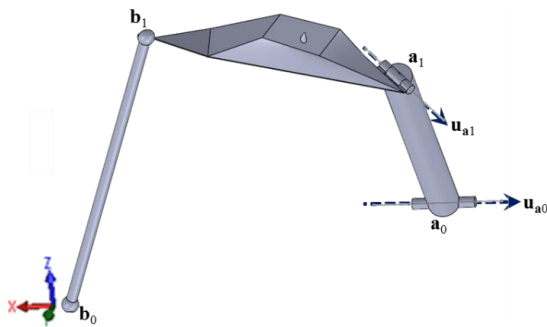|	Crank Static Torque [lbf.in]	Crank Deflection [in]	Follower-Link Load [lbf]
Pose 1	268	0.0420	32
Pose 2	171	0.0297	34
Pose 3	53	0.0135	38
Pose 4	54	0.0078	42
Pose 5	147	0.0273	43
Pose 6	220	0.0438	38
Pose 7	268	0.0595	25
Pose 8	299	0.0602	7

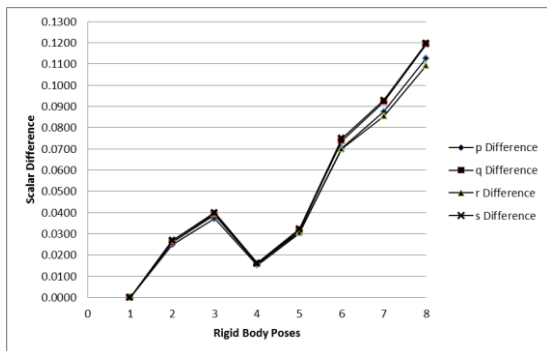**Figure 6.** Synthesized RRSS motion generator

Figure 7. Rigid-body differences (between prescribed and achieved poses) for the synthesized mechanism

The length L_1= 9.4915 in is required to satisfy the transverse deflection condition for link $\mathbf{a}_0\mathbf{a}_1$ and to result in a safe buckling load of 3430 lbs. The follower buckling load is 214 lbs. For the derivation of equation (11), the weights of the crank and follower links are assumed to be negligible. However, for the RRSS mechanism, the body force of the crank and follower should be minuscule in comparison to the applied force **F**. ADAMS dynamic modeler was used to independently confirm the achieved rigid-body positions, driver static torques, and reaction loads of the synthesized mechanisms. The mechanism solution loci were calculated in MathCAD and expressed to four decimal places.

8. Combination of Shoulder Exoskeleton and Human Model

The Amalgamation of the whole-body model and rehabilitation exoskeleton mechanism, which includes RRSS linkage, coupler extension, and base (Figure 9), was built using ADAMS. The coupler was adjusted to fit over the arm (Figure 9a). Figures 9b and 9c show the generated curve from tracing point X; where point X is an arbitrary point located at the very corner of the arm coupler. The figures (9b and 9c) also show the body poses 1 through 8, respectively. The arm weight in addition to the coupler extension will always be in the z-axis direction (i.e. gravity). The path of point X is partial of circumduction motion in 3-D; the motion starts at pose 1 (Figure 9b). As the RRSS mechanism starts the motion, the shoulder moves passively and triggers glenohumral (GH) joint movement (flexion), as the motion continues further up and outward (abduction), scapula-thoracic movement comes (pose 8, Figure 9c).

RRSS mechanism motion employs many muscles contributing to circumduction motion ($120°$ in flexion and $120°$ abduction). Hence, with special geometrical modifications and arrangements to the coupler extension, rehabilitation of muscle motor skills to conduct a full range of movements can be expedited.
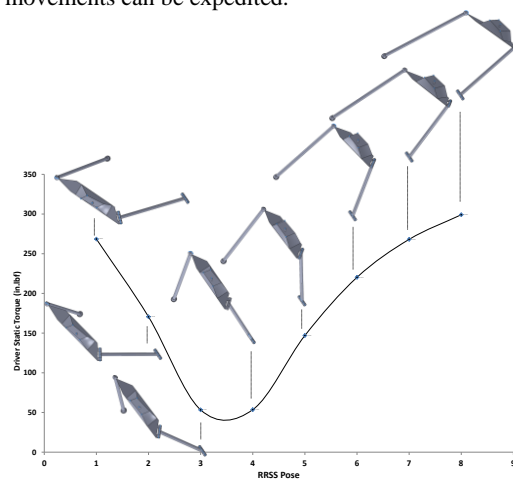

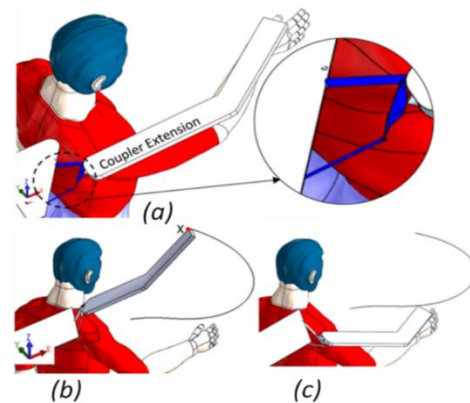**Figure 8.** Magnitude of the driver static torque T for the specified crank rotation

Figure 9. Isometric view of human model and RRSS mechanism, a) general and detailed view of RRSS mechanism and coupler extension, b) tracing path of point "X", coupler extension at pose 8, and c) coupler extension at pose 2.

Shoulder motion includes many synovial joints; GH, acromioclavicular (AC), scapulothoracic (ST), and sternoclavicular (SC), these constitute very complex motion of the shoulder joint. For simplicity, the most compelling motion in the shoulder joint (i.e.GH) will be considered. The joint is marked with a cross sign in Figure 10. Due to the pose displacement of the RRSS mechanism, the coupler extension will create a workspace region (blue) as shown in

Figure 10a-10c, this region passes through workspace volumes 1,4,5 and 7 as calculated by [49-50]. Therefore, in Figure 10d, the motion in workspace volumes 1.2.3.4, 1.4.5.7, or 3.4.7 parallel or semi-parallel to human planes sagittal, coronal or transverse respectively, is considered as circumduction motion. Through mobilization effort post-stroke, shoulder repositioning in several circumductionmotions in any/all workspace volume will greatly improve occupational functions of the shoulder and arm. The circumduction motion of the arm and shoulder is proved by the kinostatic optimization carried out for the conceptual design of the RRSS mechanism with arm extension.
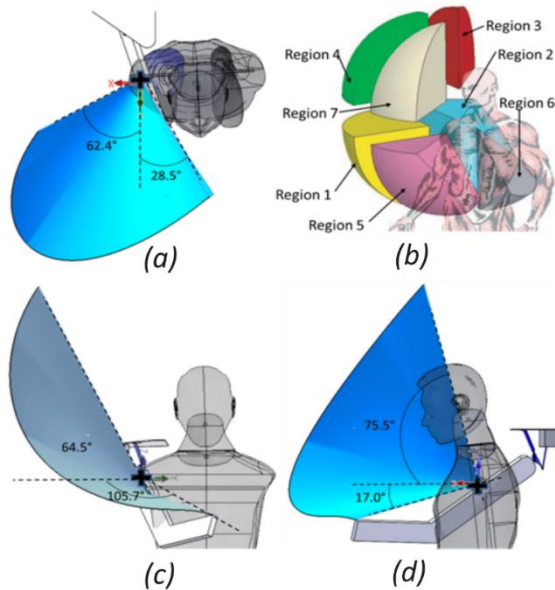

Figure 10. Workspace region for coupler extension of RRSS mechanism normal to a) transverse plane view, b) coronal plane view c) sagittal plane view, and d) workspace volume of shoulder and arm as calculated by [49-50]

9. Conclusion

The main objective of this work is to design a shoulder-arm rehabilitation exoskeleton. This will give hope to those who are suffering from low upper extremities motor skills performance, especially stroke patients, to use their extremities effectively. This design will also reduce the time of the rehabilitation process to recover the powerful efficiency of the upper extremities.

The driver link static torque constraint was formulated in this work. When incorporated into a conventional RRSS mechanism motion generation model, the resulting model was demonstrated to be effective in calculating spatial RRSS motion generator solutions that approximate the prescribed rigid-body positions and satisfy driver link static torque and coupler load constraints. It was also demonstrated that the torque constraint could be used with the spatial RRSS motion generation model and solved using a commercial goal program solver such as MathCAD. Several levels of simulations, modeling, and programming tools, in addition to MathCAD, were used to support this research: Anybody software has been used as a musculoskeletal analysis tool, SolidWorks for modeling, ADAMS for multi-body dynamics, and Computer-Aided

Drafting software for helping to provide the initial guesses for SQP.

References

[1] P. Garrec, J.P. Friconneau, Y. Measson, Y. Perrot. Able, "An innovative transparent exoskeleton for the upper-limb", IEEE/lRSJ International Conference on Intelligent Robots and Systems, Sept. 2008, pp. 1483-1488.

[2] N. Tobias, M. Mihelj, R. Riener, "ARMin: A Robot for Patient-Cooperative Arm Therapy", Journal of Medical and Biological Engineering and Computing, Vol. 45, No. 9, 2007, pp. 887-900.

[3] H. A. Stienen, E. E. G. Hekman, F. C. T Van der Helm, G. B. Prange, M. J. A. Jannink, A. M. M. Aalsma, H. Van der Kooij, "Dampce: dynamic force-coordination trainer for the upper extremities", IEEE 10th International Conference on Rehabilitation Robotics, ICORR 2007, pp. 820-826.

[4] H. A. Stienen, E. E. G. Hekman, H. ter Braak, A. M. M. Aalsma, F. C. T. van der Helm, H. Van der Kooij, "Design of rotational hydro-elastic actuator for an active upper-extremity rehabilitation exoskeleton", 2nd IEEE RAS EMBS International Conference on Biomedical Robotics and Biomechatronics, BioRob 2008, pp. 881-888.

[5] T. Nef, M. Mihelj, G. Kiefer, C. Perndle, R. Muller, R. Riener, "ARMin – Exoskeleton for Arm Therapy in Stroke Patients", IEEE 10th International Conference on Rehabilitation Robotics, ICORR 2007, pp. 68-74.

[6] H.Masur, "The Rational Use of Robots in Neurorehabilitation – Fact or Fiction?", Deutsches Arzteblatt, Vol. 105, No. 18, 2008, pp. 329.

[7] J. C. Perry, J. Rosen, S. Burns, "Upper-Limb Powered Exoskeleton Design", IEEE/ASME Transaction on Mechatronics, Vol. 12, 2007, pp. 408-417.

[8] N. G. Tsagarakis, D. G. Caldwell, "Development and Control of a 'Soft-Actuated' Exoskeleton for Use in Physiotherapy and Training", Autonomous Robots, Vol. 15, 2003, pp. 21-33.

[9] Gupta, M. K. O'Malley, V. Patoglu, C. Burgar, "Design, Control and Performance of Rice Wrist: A Force Feedback Wrist Exoskeleton for Rehabilitation and Training", International Journal of Robotics Research, Vol. 27, The Netherlands, 2008, pp. 233-251.

[10] R. C. V. Loureiro, W. S. Harwin, "Reach & Grasp Therapy: Design and Control of a 9-DOF Robotic Neuro-rehabilitation System", IEEE International Conference on Rehabilitation Robotics, Noordwijk, 2007, pp. 757-763.

[11] K. Yamamoto, M. Ishii, H. Noborisaka, K. Hyodo, "Stand Alone Wearable Power Assisting Suit: Sensing and Control Systems", IEEE International Workshop on Robot and Human Interactive Communication, Kurashiki, Okayama, Japan, 2004.

[12] E. T. Wolbrecht, D. J. Reinkensmeyer, J. E. Bobrow, "Pneumatic Control of Robots for Rehabilitation," International Journal of Robotics Research, Vol. 29, 2012, pp. 23-38.

[13] J. Oblak, I. Cikajlo, Z. Matjacic, "Universal Haptic Drive: A Robot for Arm and Wrist Rehabilitation," IEEE Transactions on Neural Systems and Rehabilitation Engineering, Vol. 18, 2010, pp. 293-302.

[14] S. H. Ameen, R. K. Hussain, R. R. K. Al-Arkawazi, "A Novel Design of the Articulated Lower Limb Prosthetic Foot Using Fiber-Reinforced Polymer", Jordan Journal of Mechanical and Industrial Engineering, Vol. 14, No. 4, 2022, pp. 581-599.

[15] M. Vukobratovic, D. Hristic, Z. Stojiljkovic, "Development of Active Anthropomorphic Exoskeletons", Medical and Biological Engineering and Computing, Vol. 12, 1974, pp. 66-80.

[16] B. Zoss, H. Kazerooni, A. Chu, "Biomechanical Design of the Berkeley Extremity Exoskeleton (BLEEX)", IEEE/ASME Transaction on Mechatronics, Vol. 11, 2006, pp. 128-138.

[17] G. Aguirre-Ollinger, J. E. Colgate, M. A. Peshkin, A. Goswami, "Design of an Active One-Degree-of-Freedom Lower-Limb Exoskeleton with Inertia Compensation", International Journal of Robotics Research, 2010.

[18] V. Sharma, D. B. McCreery, M. Han, V. Pikov, "Bidirectional Telemetry Controller for Neuroprosthetic Devices", IEEE Transactions on Neural Systems and Rehabilitation Engineering, Vol.18, 2012, pp. 67-74.

[19] Schiele, F. C. T. van der Helm, "Kinematic Design to Improve Ergonomics in Human Machine Interaction", IEEE Transactions on Neural Systems and Rehabilitation Engineering, Vol. 14, 2006, pp. 456-469.

[20] N. Jarrassé, G. Morel, "A Formal Method for Avoiding Hyperstaticity When Connecting an Exoskeleton to a Human Member", IEEE International Conference on Robotics and Automation (ICRA), Anchorage, AK, USA, 2010, pp. 1188-1195.

[21] K. Kong, H. Moon, B. Hwang, D. Jeon, M. Tomizuka, "Robotic Rehabilitation Treatments: Realization of Aquatic Therapy Effects in Exoskeleton Systems", IEEE International Conference on Robotics and Automation (ICRA), Kobe, Japan, 2009, pp. 1923-1928.

[22] Duschau-Wicke, J. v. Zitzewitz, A. Caprez, L. Lünenburger, Robert Riener, "Path Control: A Method for Patient-Cooperative Robot-Aided Gait Rehabilitation", IEEE Transactions on Neural Systems and Rehabilitation Engineering, Vol. 18, 2012, pp. 38-48.

[23] J. Klein, S. Spencer, J. Allington, J. E. Bobrow, D. J. Reinkensmeyer, "Optimization of a Parallel Shoulder Mechanism to Achieve a High-Force, Low-Mass, Robotic-Arm Exoskeleton", IEEE Transactions on Robotics, vol. 26, 2010, pp. 710-715.

[24] S. Mutawe, M. Hayajneh, S. Banihani, M. Al Qaderi, "Simulation of Trajectory Tracking and Motion Coordination for Heterogeneous Multi-Robots System", Jordan Journal of Mechanical and Industrial Engineering, Vol. 15, No. 4, 2021, pp. 337-345.

[25] Y. Ren, J. Liu, "Automatic Obstacle Avoidance Path Planning Method for Unmanned Ground Vehicle Based on Improved Bee Colony Algorithm", Jordan Journal of Mechanical and Industrial Engineering, Vol. 16, No. 1, 2022, pp. 11-18.

[26] Y. Li, "Design of Path Tracking Control System for UAV Based on Adaptive Preview Method", Jordan Journal of Mechanical and Industrial Engineering, Vol. 14, No. 1, 2020, pp. 101-108.

[27] Y. M. Al-Smadi, K. Russell, R. S. Sodhi, "On Traveler Braking Mechanism Design with Elastic Deflection and Buckling Considerations," Journal of Mechanics Based Design of Structures and Machines, Vol. 37, No. 3, 2009, pp. 401-412.

[28] Y. M. Al-Smadi, K. Russell, R. S. Sodhi, "Four-bar motion generation with elasticity constraints and optimization", Journal of Multi Body Dynamics, Vol. 223, 2009, pp. 245-253.

[29] K. Russell, Q. Shen, W. T. Lee, R. S. Sodhi, "On the Synthesis of Spatial RRSS Motion Generators with Prescribed Coupler Loads", Journal of Advanced Mechanical Design, Systems, and Manufacturing, Vol.3, 2009, pp. 236-244.

[30] S. Haijun, C. L. Collins, M. J. McCarthy, "Classification of RRSS Linkages", Mechanism and Machine Theory, Vol. 37, 2002, pp. 1413-1433.

[31] K. Lee, Y. Yoon, "Kinematic Synthesis of RRSS Spatial Motion Generators Using Euler Parameters and Quaternion Algebra", Proceedings of the Institution of Mechanical Engineers, Part C," Journal of Mechanical Engineering Science, Vol. 207, 1993, pp. 355-359.

[32] K. Al-Widyan, Xiao Qing Ma, J. Angeles, "The robust design of parallel spherical robots", Mechanism and Machine Theory, Vol. 46, 2011, pp. 335-343.

[33] Z. Meng, "Trajectory Tracking Control Algorithm of Six Degrees of Freedom Industrial Robot", Jordan Journal of Mechanical and Industrial Engineering, Vol. 16, No. 1, 2022, pp. 97-104

[34] P. Zhao, "Moving Trajectory Tracking Method of Multi Degree of Freedom Manipulator Based on Particle Filter Algorithm", Jordan Journal of Mechanical and Industrial Engineering, Vol. 16, No. 4, 2022, pp. 591-600.

[35] J. Li, "A New Trajectory Planning Method of 6-DOF Apple Picking Manipulator", Jordan Journal of Mechanical and Industrial Engineering, Vol. 16, No. 5, 2022, pp. 777-785

[36] Hashlamon, "Adaptive Disturbance Estimation and Compensation for Delta Robots", Jordan Journal of Mechanical and Industrial Engineering, Vol. 14, No. 4, 2020, pp. 413-422.

[37] J. Gong, W. Wei, S. Peng, K. Zhang, "Analytical Formula of Positive Position Solution of 2PPa-PSS 3- Translational Parallel Mechanism with Low Coupling-degree and its Numerical Application", Jordan Journal of Mechanical and Industrial Engineering, Vol. 15, No. 5, 2021, pp. 419-429.

[38] Qaiyum, A Mohammad, "A novel approach for optimal synthesis of path generator four-bar planar mechanism using improved harmony search algorithm", Australian Journal of Mechanical Engineering, Vol. 22, No. 1, 2024.

[39] S. Nguyen-Van, Q. X. Lieu, N. Xuan-Mung,T. T. Nguyen, "A new study on optimization of four-bar mechanisms based on a hybrid-combined differential evolution and Jaya algorithm", Symmetry 14(2), 2022, Special Issue Unmanned Vehicles, Automation, and Robotics.

[40] S. El-Skakery, R. Ramadan, K. Khader, "Analytical and Graphical Optimal Synthesis of Crank-Rocker Four Bar Mechanisms for Achieving Targeted Transmission Angle Deviations", Jordan Journal of Mechanical and Industrial Engineering, Vol. 14, No. 3, 2021, pp. 303-313.

[41] W. T. Lee, Y. M. Al-Smadi, K. Russell, "A dual cam system for four-bar motion generation with adjustable length crank and follower links", Journal of Advanced Mechanical Design, Systems, and Manufacturing. Vol.15, No.6, 2021.

[42] Suh, C. H., Radcliffe C.W. Kinematics and Mechanism Design. New York: John Wiley and Son Inc., 1978.

[43] Huang and B. Roth, "Dimensional Synthesis of Closed-Loop Linkages to Match Force and Position Specifications", Journal of Mechanical Design, Vol. 115, No. 2, 1993, pp. 194-198.

[44] Pilkey, W. D. Formulas for stress, strain and structural matrices.New York: John Wiley and Sons Inc., 2004.

[45] A.J.M. Ferreira. MATLAB Codes for Finite Element Analysis: Solids and Structures, Solid Mechanics and Its Applications, Vol. 157, Springer, 2009.

[46] Ziemian, Ronald D. Guide to Stability Design Criteria for Metal Structures.New York: John Wiley and Sons Inc., 2010.

[47] S. P. Han, "A globally convergent method for nonlinear programming. Journal of Optimization and Theory Applications", Vol. 22, 1977, pp. 297-309.

[48] M. J. D. Powell, "A fast algorithm for nonlinearly constrained optimization calculations", Numerical analysis, lecture notes in mathematics (Ed. G. A. Watson), Vol. 630, 2006, (Springer-Verlag, Berlin, Germany), pp. 144-157.

[49] G. Yang, S.K. Mustafa, S.H. Yeo, W. Lin, W.B. Lim, "Kinematic design of an anthropomimetic 7-DOF cable-driven robotic arm", Frontiers of Mechanical Engineering, Vol. 6, No. 1, 2011, pp. 45–60.

[50] S.K. Mustafa, S.H. Yeo, C.B. Pham, G. Yang, W. Lin, "A biologically-inspired anthropocentric shoulder joint rehabilitator: workspace analysis & optimization", IEEE International Conference Mechatronics and Automation, Niagara Falls, Canada, 2005.